Materials and Design 90 (2016) 185–195

Contents lists available at ScienceDirect

Materials and Design

journal homepage: www.elsevier.com/locate/jmad

Fabrication of vertically aligned carbon nanotubes–zinc oxide nanocomposites and their field electron emission enhancement

A.B. Suriani [a,b,*], A.R. Dalila [a,b], A. Mohamed [a,c], M.H. Mamat [d], M.F. Malek [d,e], T. Soga [f], M. Tanemura [f]

[a] Nanotechnology Research Centre, Faculty of Science and Mathematics, Universiti Pendidikan Sultan Idris, 35900 Tanjung Malim, Perak, Malaysia
[b] Department of Physics, Faculty of Science and Mathematics, Universiti Pendidikan Sultan Idris, 35900 Tanjung Malim, Perak, Malaysia
[c] Department of Chemistry, Faculty of Science and Mathematics, Universiti Pendidikan Sultan Idris, 35900 Tanjung Malim, Perak, Malaysia
[d] NANO-ElecTronic Centre (NET), Faculty of Electrical Engineering, Universiti Teknologi MARA (UiTM), 40450 Shah Alam, Selangor, Malaysia
[e] NANO-SciTech Centre (NST), Institute of Science (IOS), Universiti Teknologi MARA (UiTM), 40450 Shah Alam, Selangor, Malaysia
[f] Department of Frontier Materials, Nagoya Institute of Technology, Gokiso-cho, Showa-ku, Nagoya 466-8555, Japan

ARTICLE INFO

Article history:
Received 29 July 2015
Received in revised form 11 October 2015
Accepted 12 October 2015
Available online 23 October 2015

Keywords:
Carbon nanotubes
Zinc oxide
Nanocomposites
Field electron emission

ABSTRACT

Systematic investigation on the fabrications of vertically aligned carbon nanotubes (VACNTs) and zinc oxide (ZnO) nanocomposites for two different configurations were performed to enhance the field electron emission (FEE) performance of the VACNTs synthesised from waste chicken fat. FEE tests demonstrated improvement with the addition of ZnO nanostructures under the VACNT array, where the emission current increased from 212.85 to 259.80 μAcm^{-2}, while the turn-on field reduced from 2.66 to 1.60 $V\mu m^{-1}$. Meanwhile, the growth of ZnO nanostructures on top of the VACNTs array resulted in a tremendous increase in emission current of up to 2090.00 μAcm^{-2} and a decrease in the turn-on field to 0.49 $V\mu m^{-1}$. The difference in the FEE improvement by different composite configuration reflects the significant role of the composite order. The improvement of FEE is influenced by the geometrical shape of the emitters as well as tunnelling effect of electrons through the structure of nanocomposite.

1. Introduction

Carbon nanotubes (CNTs) and zinc oxide (ZnO) are widely known as potential electron emitters due to their high performance in field emission. However, both materials suffer from several key disadvantages, which have inhibited the use of these materials as electron emitters in practical electronic applications. On one hand, some disadvantages related to CNTs are as follows: CNTs degrade in oxygenated environments [1], CNTs become welded with the neighbouring nanotubes due to superheating effect [2], and the dense distribution of the CNT tips results in generating a high field screening effect [3]. On the other hand, ZnO material is unable to sustain large current densities [4]. Therefore, the composite of these two superior materials is expected to reinforce their beneficial properties, hence enhancing the field emission ability.

Both theoretical and experimental outcomes have confirmed the improvement of the field emission properties through the fabrication of CNTs and ZnO composites [2,5–12]. Low turn-on fields were observed in the composite of CNT/ZnO nanowires [9] due to the combined effect of field enhancement from the CNTs and the ZnO. Yan, Tay, and Miele [2] achieved a low operating electric field and stable field emission via ordered CNT-ZnO heterojunction arrays, where the ZnO nanowires were grown on aligned arrays of CNTs. Yu et al. [10] reported the low turn-on and threshold field from ZnO nanomultipods grown on a film of multi-walled CNTs. Meanwhile, a large enhancement of the field emission of ZnO was reported by Liu et al. [11] by growing the CNTs onto ZnO nanorods in ring patterned arrays. Li et al. [12] observed stable emission with a fluctuation of up to 5% and a significant enhancement relative to ZnO nanorods from CNT bundle arrays grown on self-aligned ZnO nanorods. The common element that induced the enhancement in all these previous findings is actually the order of the configuration, in which the material that assists the improvement in the field emission was placed at the top of the composite. Alternatively, Zhang et al. [13] reported a different approach, in which the field emission of CNTs can be enhanced by depositing the CNTs onto metal films. The results of that study implied that the field emission performance is assisted by the metal films under the CNTs by reducing the width of the interface barrier between CNTs and the substrate [13].

However, these studies [2,5–13] focused only on the improvement of FEE using single layer configuration. To the best of our knowledge, this is the first report on the FEE of the VACNTs synthesised using waste chicken fat and the method of enhancing the FEE performance using two different configurations of nanocomposite with ZnO in vice-versa order. The band structures of both nanocomposite configurations were also presented to assist the investigation of the electron emission mechanism. The VACNTs were synthesised using a low-cost carbon precursor, i.e., waste chicken fat [14–16], via a thermal chemical vapour deposition (TCVD) method while the ZnO nanostructures were

* Corresponding author.
E-mail address: absuriani@yahoo.com (A.B. Suriani).

http://dx.doi.org/10.1016/j.matdes.2015.10.051
0264-1275/

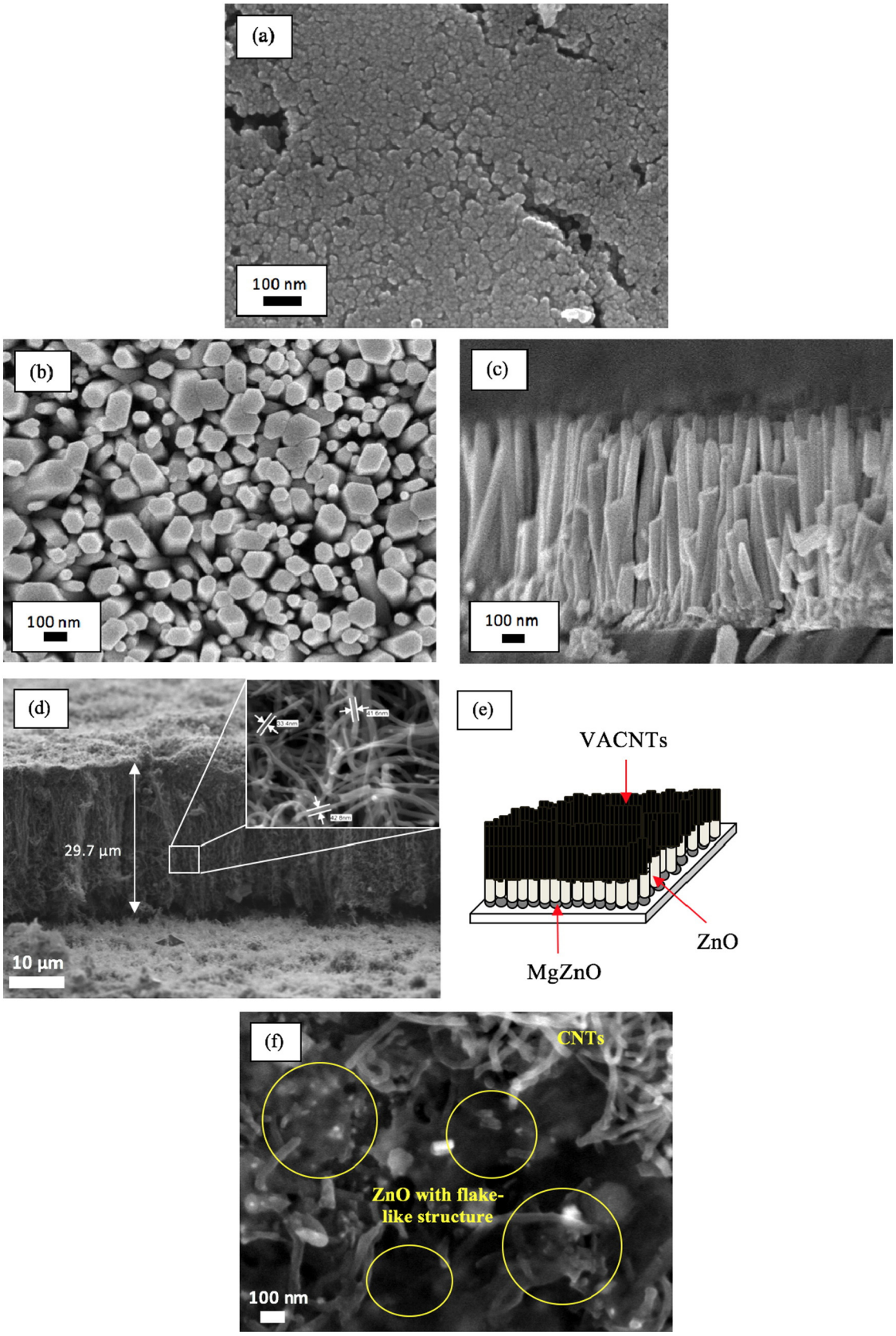

Fig. 1. FESEM images of (a) the MgZnO seed layer deposited by the spin coating technique; (b) top and (c) side view of the ZnO nanostructure synthesised using the sol-gel immersion method; and (d) ZnO–VACNTs nanocomposite, with a high magnification image of the synthesised VACNTs shown as the inset image. Only the VACNTs were visible in the image. (e) The expected configuration of the ZnO–VACNTs nanocomposite. (f) High magnification FESEM image showing that only flake-like structures and CNTs remain on the substrate, instead of ZnO nanorods, after the CNTs were synthesised on top of the ZnO layer. (g) TEM and (h) HR-TEM images of the ZnO–VACNTs nanocomposite.

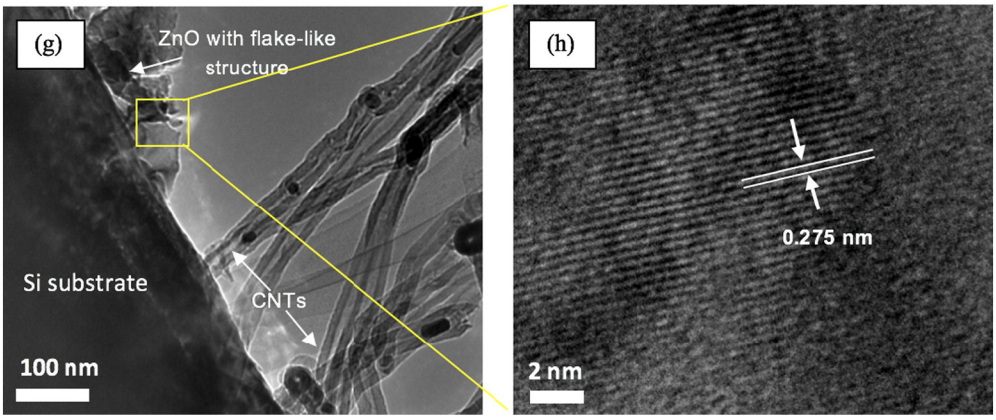

Fig. 1 (*continued*).

synthesised using the sol–gel method [17] that can be performed at low temperature and pressure. The structural and field emission properties of VACNT/ZnO nanocomposites were systematically investigated using field emission scanning electron microscopy (FESEM), high resolution transmission electron microscopy (HRTEM), energy-dispersive X-ray spectroscopy (EDX), X-ray diffraction (XRD), and micro-Raman microscopy.

2. Materials & methods

For the ZnO–VACNT nanocomposite configuration (VACNTs grown on top of ZnO nanostructures), the fabrication started with the deposition of a thin magnesium zinc oxide (MgZnO) layer on p-type Si substrates (2×2 cm^2) using the spin coating method. ZnO nanostructures were then grown on MgZnO-coated Si substrates via an immersion method. The procedures of the spin coating and the immersion method were similar to those of previous reports [18–20]. Afterwards, the VACNTs were synthesised using the oil extracted from the waste chicken fats in a double-stage TCVD furnace. The synthesis and precursor vaporisation temperatures were set to 800 and 570 °C, respectively, and the synthesis process was similar to that previously reported [14,21–24].

Meanwhile, the fabrication of VACNT–ZnO nanocomposites was in reverse order to the above configuration, where the VACNTs were initially synthesised, followed by the deposition of MgZnO and the growth of ZnO. The samples were characterised using FESEM-JEOL 7100F, EDX-

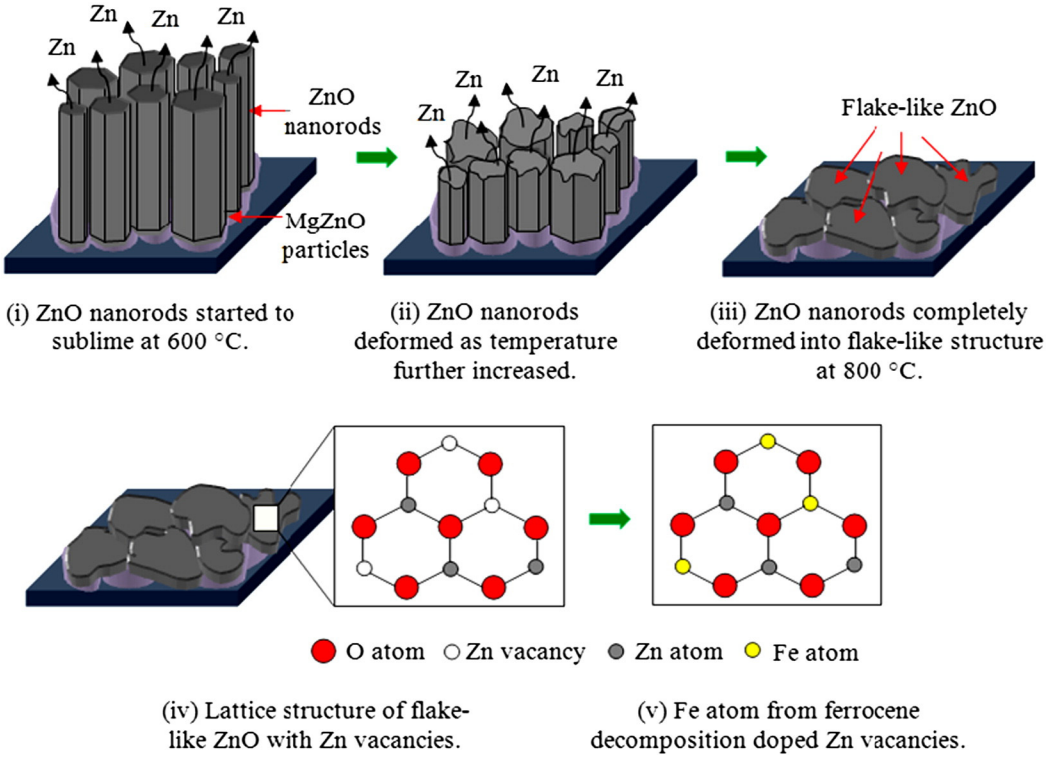

Fig. 2. (i) At the synthesis temperature of 600 °C, ZnO nanorods started to sublime; (ii) ZnO nanorods deformed as the synthesis temperature increased; (iii) at 800 °C, the ZnO nanorods completely deformed into a flake-like structure; (iv) the ZnO lattice structure of flake-like ZnO with Zn vacancies as a result of sublimation; (v) the Fe atoms from ferrocene decomposition doped Zn vacancies.

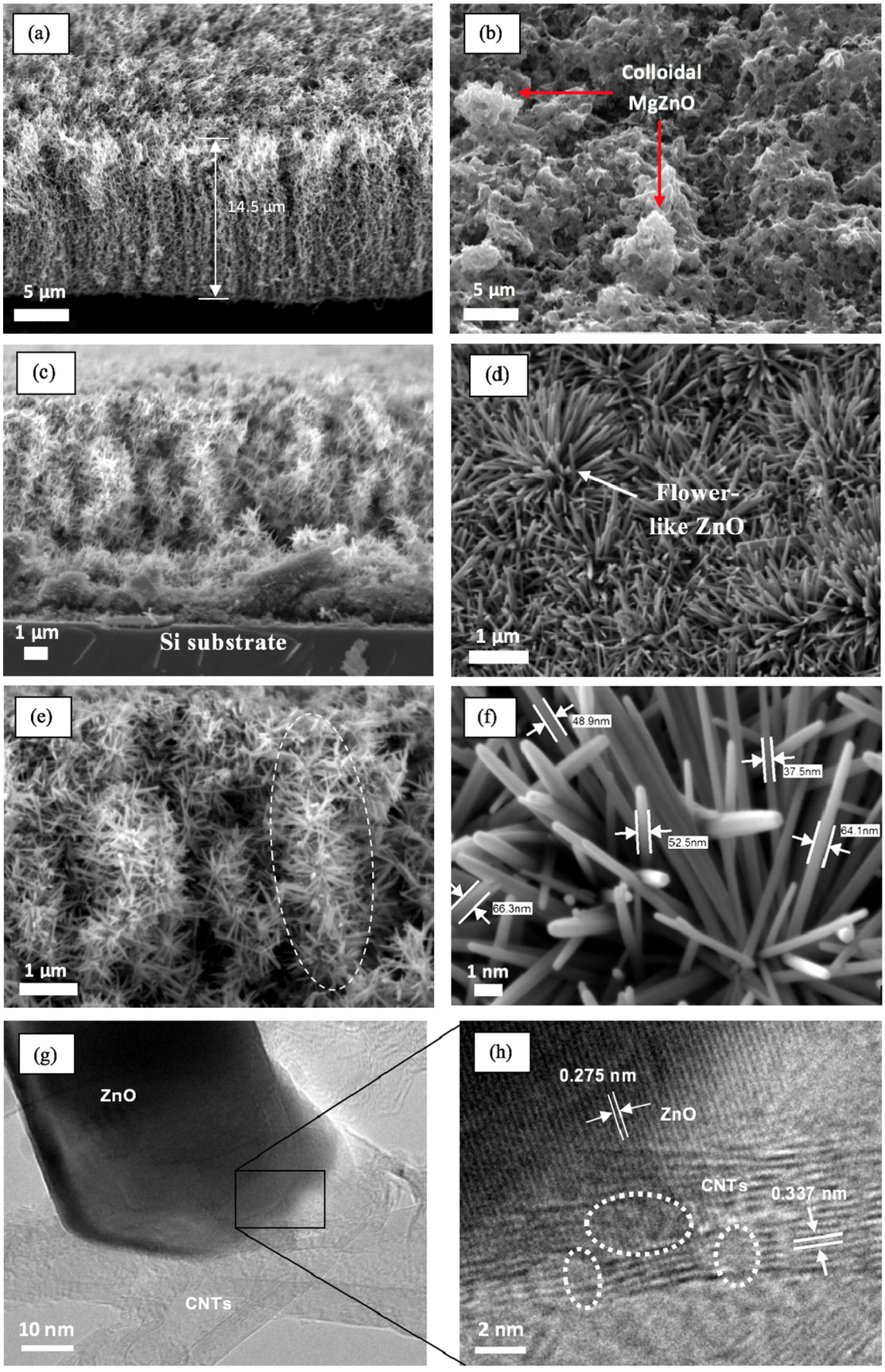

Fig. 3. (a) VACNTs synthesised; (b) top view of the MgZnO deposited on the VACNTs via the spin coating technique; (c) side and (d) top view of ZnO nanorods grown on the VACNTs; (e) the ZnO growth pattern indicated that aligned morphology of the VACNTs is not disrupted by the growth of ZnO nanorods; and (f) high magnification of flower-like ZnO nanorods. (g) TEM and (h) HR-TEM images of the VACNT–ZnO nanocomposite sample, showing the defect in the CNTs structure.

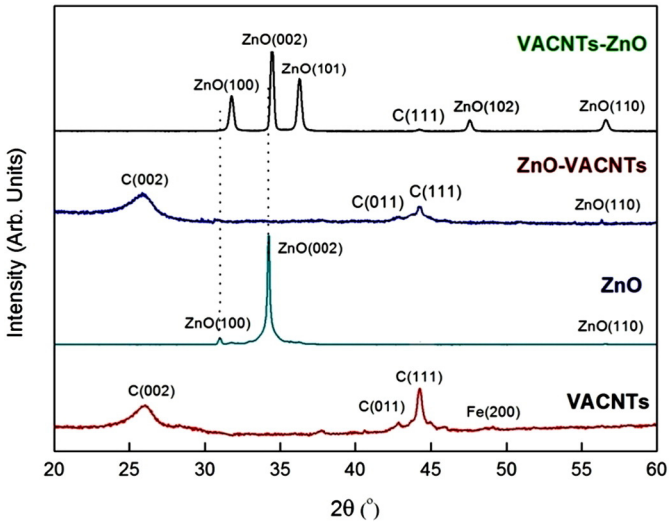

Fig. 4. XRD analysis of the VACNT–ZnO and ZnO–VACNT nanocomposites in comparison with pristine VACNTs and ZnO.

JEOL 7100F, HRTEM-JOEL JEM 2100F, XRD-Rigaku Smart Lab, and micro-Raman spectroscopy (Renishaw InVia micro Raman System). The FEE measurements were performed at 3×10^{-5} Pa in a diode configuration. The area of the electron emission was 0.1 cm^2, and the separation between electrodes was 100 μm.

3. Results & discussion

3.1. FESEM and TEM analysis

3.1.1. ZnO–VACNT nanocomposite

The surface morphology of the MgZnO seed layer grown on a Si substrate is shown in Fig. 1 (a). A uniform thin layer with grain sizes of approximately 22–36 nm was produced. The top and side views of the ZnO nanorod synthesised by sol–gel immersion method are shown in Fig. 1 (b) and (c), respectively. The top view of ZnO nanostructures shows that the as-grown ZnO primarily has hexagonal-shaped tips of different sizes, ranging from 60 to 224 nm. Meanwhile, the side view of the sample shows a high-density ZnO nanorod array along the perpendicular direction of the substrate surface, with a length of approximately 889.0 nm. The MgZnO seed particles, with a length of 142.2 nm, located under the ZnO nanorods array are also visible in the FESEM image.

Meanwhile, the surface morphology of a complete fabricated ZnO–VACNT nanocomposite is shown in Fig. 1(d). From the FESEM image, only VACNTs with diameters of approximately 33–43 nm and a length of 29.7 μm (growth rate of 0.50 μm min^{-1}) are visible. However, the image reveals that the obtained structure was slightly dissimilar to the expected configuration of the ZnO–VACNT, as shown in Fig. 1(e), due to the lack of visibility of the ZnO nanorods in Fig. 1(d). The magnified FESEM image in Fig. 1(f) revealed the presence of the flake-like structure, suggesting that the initially synthesised ZnO nanorods had deformed into a flake-like structure due to high synthesis temperature of the VACNTs (800 °C). This finding is in agreement with [25], which found that the ZnO nanorods were partially etched when the CNTs

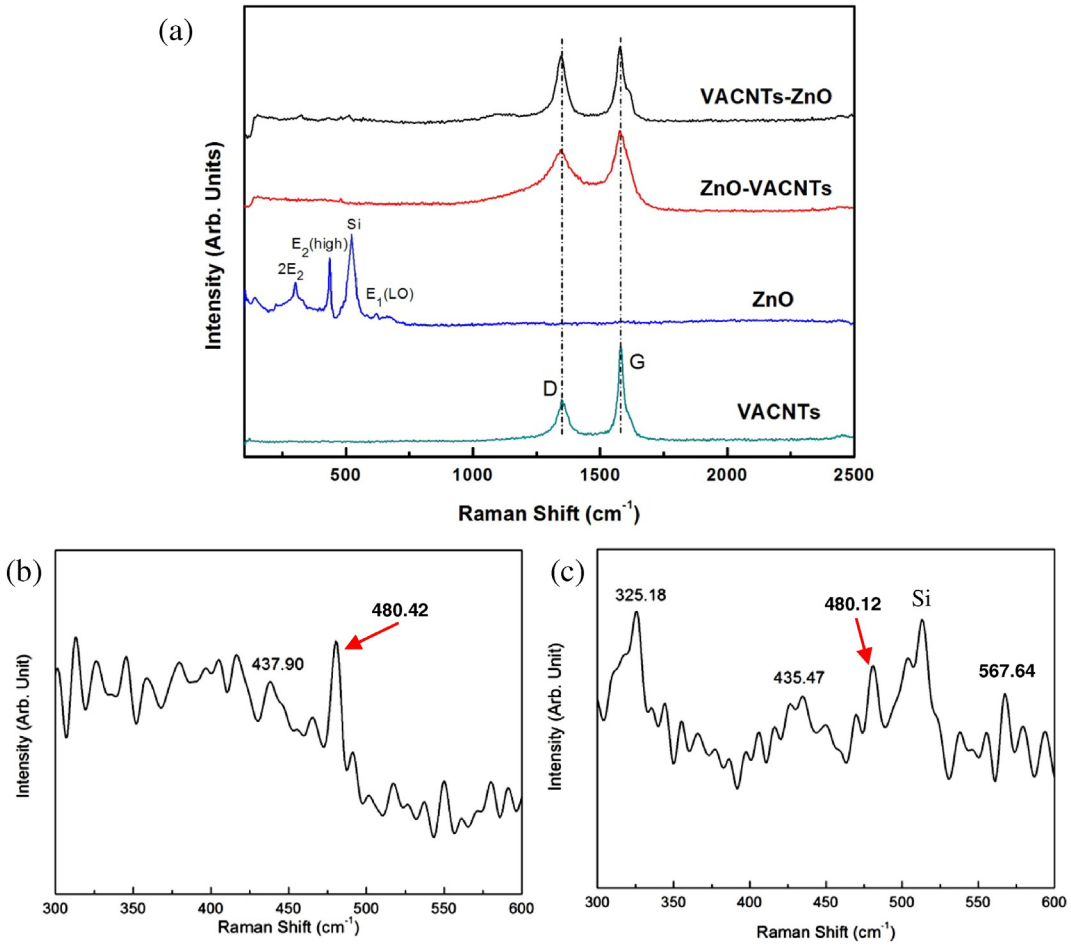

Fig. 5. (a) Micro-Raman spectra of the VACNTs, ZnO, ZnO–VACNT and VACNT–ZnO and an enlarged spectrum showing the ZnO peaks of the (b) ZnO–VACNT and (c) VACNT–ZnO samples.

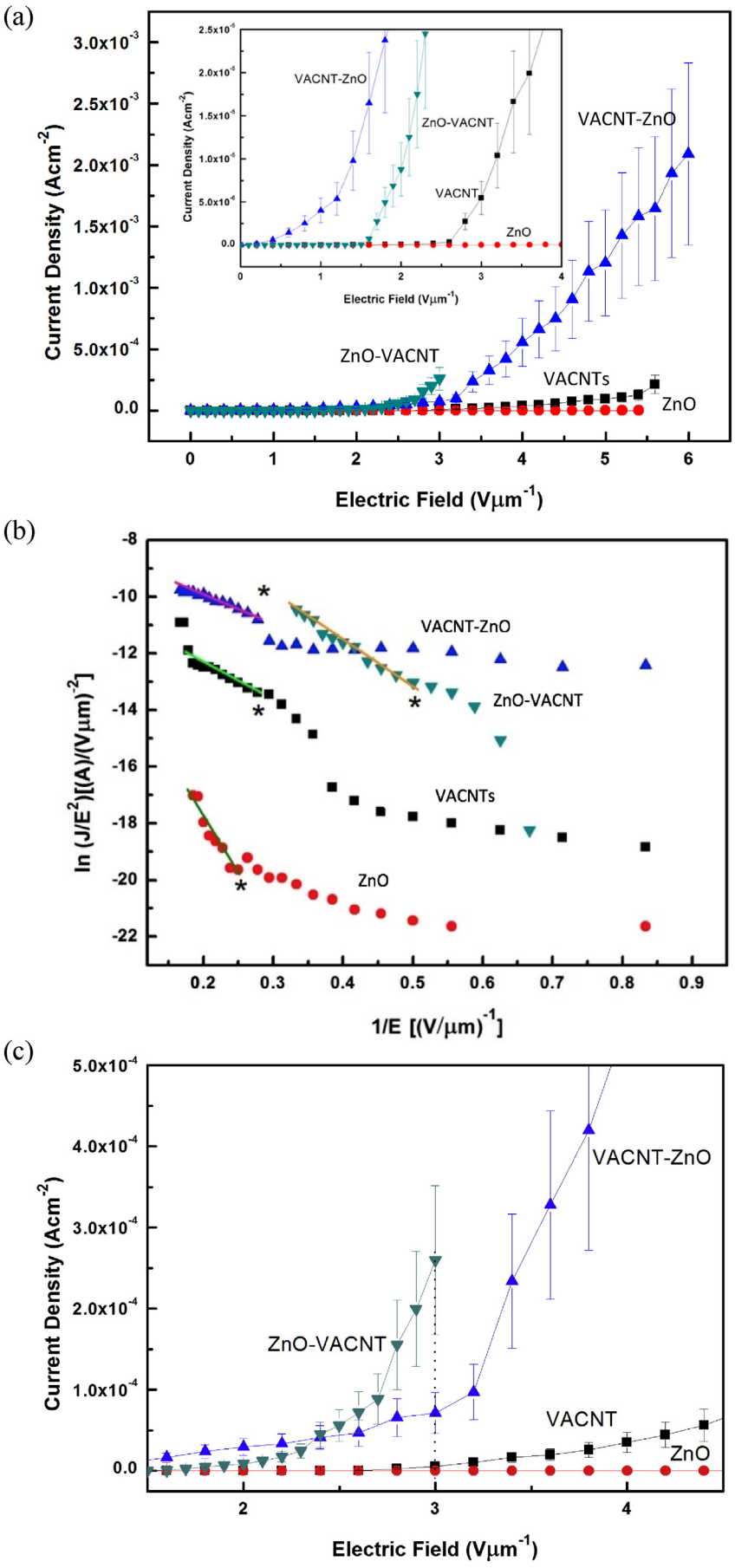
(a)
Current Density (Acm-2)
Electric Field (Vμm-1)
VACNT-ZnO
ZnO-VACNT
VACNTs
ZnO
VACNT
(b)
ln (J/E2)[(A)/(Vμm)-2]
1/E [(V/μm)-1]
(c)

were synthesised at 630–800 °C and completely etched at temperatures above 800 °C.

The length and diameters of the VACNTs synthesised on ZnO were shorter and larger, respectively, compared to the synthesised VACNTs on a bare substrate (length and diameter of 93.5 and 18.1–31.2 nm, respectively) (see the Supplementary material). This outcome was due to the lower amount of Fe catalyst deposited on top of the non-uniform surface of the flake-like ZnO structure. The low catalyst amount is a result of the sublimation of ZnO nanorods (Fig. 2(i)) that started at a temperature of 600 °C [26]. The continuous sublimation of ZnO proportional to the temperature increase induced further deformation of the ZnO nanorods (Fig. 2(ii)). The critical temperature is at 800 °C, above which the ZnO nanorods were completely deformed into a flake-like structure (Fig. 2(iii)). Furthermore, the sublimation process not only deformed the ZnO nanorods but also produced Zn vacancies in the ZnO lattice, as shown in Fig. 2(iv). The vacancies were then doped by the Fe atoms obtained from the decomposition of ferrocene (Fig. 2(v)), resulting in a reduced amount of Fe that catalyses the growth of the VACNTs.

The TEM image in Fig. 1(g) shows the flake-like structures and the CNTs that resided on the substrate. The lattice fringes of the flake-like structure are clearly observed in the HR-TEM image (Fig. 1(h)), with an interplanar spacing of 0.275 nm, which is closely matched to the *d*-spacing of (100) crystal plane (0.281 nm) of wurtzite ZnO [27]. This finding proved that the ZnO nanorods were in fact deformed and etched due to the high synthesis temperature of 800 °C and remained on a certain part of the substrate.

3.1.2. VACNT–ZnO nanocomposite

The FESEM image in Fig. 3(a) shows the VACNTs grown on the 2×2 cm^2 Si substrate with a length of 14.5 μm (growth rate of 0.24 μm min^{-1}). Fig. 3(b) shows the top view of the MgZnO deposited on the grown VACNTs. The MgZnO layer was observed to be rough and uneven compared to the MgZnO seed layer deposited on a bare substrate (Fig. 1(a)); thus, the roughness reflects the surface structure of the underlying VACNTs. MgZnO nanoparticles were also agglomerated at some areas where colloidal seed particles were formed, as shown in Fig. 3(b). The resultant agglomeration of seed particles was due to the surface tension of the solvent, which accumulated the particles during the drying process [28].

The surface morphology of ZnO nanorods synthesised on top of VACNTs is shown in Figs. 3(c)–(f). The side-view of the nanocomposite shown in Figs. 3(c)–(d) revealed that the array of VACNTs was entirely coated with the ZnO nanorods in multifarious directions. The random directions were a result of the uncontrolled orientation of the MgZnO nanocrystal seed layer on the deposited VACNTs. Moreover, the MgZnO that was in colloidal form produced nanorods with flower-like orientation (Fig. 3(d)). Note that the aligned morphology of the VACNTs is not disrupted by the growth of ZnO nanorods, as observed from the ZnO growth pattern (dotted line in Fig. 3(e)) that exhibits ZnO nanorods growing on individual nanotubes. Fig. 3(f) illustrates that the diameter of the ZnO nanorods produced is in the range of 37–66 nm, which is smaller at the tip due to the decreasing precursor concentration in the solution [29].

The HR-TEM images of the VACNT–ZnO nanocomposite sample in Figs. 3 (a)–(b)) show the interface of CNTs and ZnO nanorods, with lattice spacing of 0.275 nm for ZnO and a lattice spacing of 0.337 nm for the graphitic structure; these values are closely matched to the interplanar spacing of the wurtzite ZnO (0.275 nm) [27] and graphite structure (0.335 nm) [30], respectively. Moreover, the graphitic structure of CNTs at the ZnO–CNT interface was observed to be slightly diminished, as indicated by the dotted line in Fig. 3(b). This observation was probably due to the interactions between the ZnO precursor and the CNTs, which results in bonding at the ZnO–CNT interface and hence altering of the C–C bonds [31].

3.2. XRD analysis

Fig. 4 presents the XRD analysis of the pristine VACNTs, ZnO and VACNT/ZnO nanocomposites. The XRD pattern of the pristine VACNTs shows that the VACNTs synthesised have typical peaks of carbon at 26.03°, 42.87°, and 44.27° corresponding to the (002), (011) and (111) planes. A weak Fe peak was also detected at 48.9°, corresponding to the (200) plane. In spite of a relatively weak peak, the presence of Fe that originated from ferrocene decomposition could be confirmed. Meanwhile, the XRD pattern of pristine ZnO exhibits a sharp and most intense diffraction peak at 34.18°, corresponding to the reflection from the (002) plane. This observation indicates that the pristine ZnO has a high degree of crystallinity and grew primarily along the *c*-axis. This result is in good agreement with the FESEM observation of Section 3.1. Weak characteristic peaks located at 30.99° and 56.59°, which are related to the reflection of (100) and (110) planes, respectively, were also obtained. All the diffraction peaks obtained are indexed as the hexagonal wurtzite phase of ZnO [32]. No characteristic peaks of other impurities, such as $Zn(OH)_2$, were detected, which indicates that only single-phase ZnO samples were formed [33].

For the ZnO–VACNT sample, the carbon peaks of the (002), (110) and (111) planes located at 25.95°, 42.87°, and 44.27°, respectively, were accompanied by a weak ZnO peak of (110) at 56.35°, which represents the co-existence of phase of CNTs and ZnO. No ZnO peak of the (002) plane was detected, which reaffirms that the ZnO nanorods that were initially grown had deformed and become etched due to the high synthesis temperature of CNTs. Note that the carbon peak of (111) had a lower intensity than the peak of pristine VACNTs, which exhibits a lower degree of crystallinity for VACNTs that grow on top of ZnO nanostructure. This result was attributed to the lower amount of Fe catalyst utilised for the growth of VACNTs because a partial amount of Fe had doped the Zn vacancies, while the rest of the Zn vacancies were not doped, resulting in an imbalanced ratio of carbon atoms versus the Fe catalyst. The Fe catalyst was then unable to decompose the large amount of incoming carbon particles, resulting in encapsulation of the catalyst by thick carbon particles, thereby rendering the catalyst inactive. In addition, no iron oxide phase was observed in the XRD pattern because the Fe-doping was unable to change the structure of ZnO, which might be ascribed to the Fe embedded in the ZnO thin films that formed ordered substitutional sites within the lattice [34]. This finding was consistent with the studies of [35,36,37], which covered the effect of Fe doping in ZnO thin films.

Meanwhile, the sample of VACNT–ZnO shows a low intensity of carbon and a high intensity of ZnO peaks, which confirms the co-existence of the CNTs and ZnO in the sample. This result also confirms that the surface of the nanocomposite has a large number of ZnO nanoparticles. In contrast to the pristine vertically aligned ZnO nanorods grown on a Si substrate, with a strong reflection of the (002) plane, the VACNT–ZnO sample shows strong reflections from multiple ZnO peaks of (100), (002), and (101), located at 31.76, 34.42, and 36.25°, respectively. In addition, reflections from the (102) and (110) planes at 47.56 and 56.62°, respectively, were also detected. The presence of these multiple peaks are in agreement with the FESEM images depictured in Fig. 3, where the ZnO nanorods were observed to grow in multiple directions. In addition, the diffraction peak of the (002) plane located at 34.42° was

Fig. 6. (a) Typical *J*–*E* curves with magnified curve at the low field region and (b) F–N plots of pristine VACNTs, ZnO and VACNT/ZnO nanocomposite samples. (c) Enlarged *J*–*E* curve of all samples, showing the dramatic increase in the emission current of the ZnO–VACNT sample.

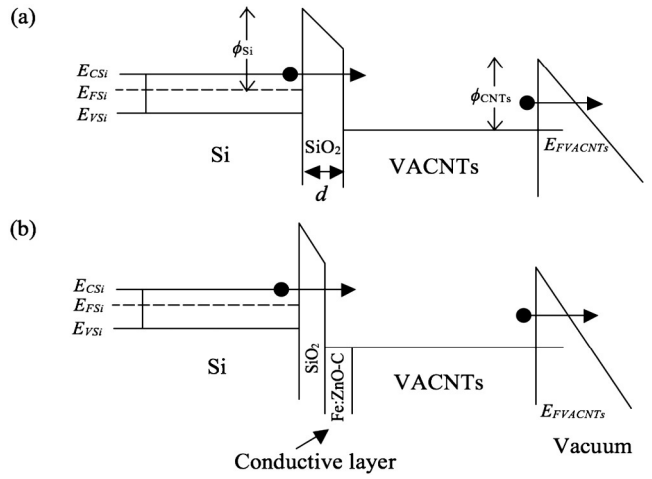

Fig. 7. Band diagrams of (a) pristine VACNTs and (b) ZnO–VACNT samples, illustrating that the addition of the Fe:ZnO-C alloy layer reduces the substrate–VACNT barrier.

found to be minimally shifted by approximately 0.22° compared to the pristine ZnO diffraction peak of 34.20°. This shift was due to the presence of carbonaceous material, which changed the ZnO lattice constant [38].

3.3. Micro-Raman analysis

Micro-Raman spectra for pristine VACNTs and ZnO as well as nanocomposites of VACNT–ZnO and ZnO–VACNT samples are shown in Fig. 5 (a). The D and G peaks located at approximately 1349 and 1580 cm^{-1}, respectively, are shown in the micro-Raman spectrum of pristine VACNTs, while the I_D/I_G ratio that indicates the crystallinity of the sample was found to be 0.39. Meanwhile, the micro-Raman spectrum of pristine ZnO sample shows intense characteristic peaks of ZnO located at 436.99, 583.42, and 326.00 cm^{-1}, corresponding to $2E_2$, E_2 (high), and E_1 (LO), respectively. The $2E_2$ and E_2 (high) are attributed to the peak characteristic of a wurtzite phase, while E_1 (LO) is related to the formation of defects in the nanorods [39].

For ZnO–VACNT sample, the D and G peaks were found to be slightly shifted towards lower wavenumbers of 1344.18 and 1577.40 cm^{-1}, respectively. The shift occurred due to the chemical interaction between CNTs and ZnO nanostructures [40]. The value of the I_D/I_G ratio was 0.65, which indicates the reduction in crystallinity compared to pristine VACNTs. This result is consistent with the XRD result of this sample. The reduction of the crystallinity of the CNTs was due to the lower amount of Fe catalyst to catalyse the growth of CNTs because a partial amount of Fe had initially diffused into the Zn vacancies. The reduced amount of catalyst remaining could not completely decompose the large amount of carbon particles; hence, low-quality CNTs were produced. Meanwhile, only a faint ZnO characteristic peak located at 437.90 cm^{-1} was detected in the sample (Fig. 5(b)). The faint peak indicates the low crystallinity of the synthesised ZnO, which is attributed to the deformation of ZnO nanorods due to the high synthesis temperature of 800 °C applied during the synthesis of CNTs.

The D and G peaks of VACNT–ZnO sample were also slightly shifted towards lower wavenumbers of 1346.23 and 1578.42 cm^{-1}, respectively, resulting from the chemical interaction between the CNTs and ZnO nanostructures [40]. The value of I_D/I_G ratio was 0.90, which indicates a significant reduction in the crystallinity of the CNTs. This reduction arises from the interactions between the ZnO precursor and the VACNTs, which form bonds at the VACNT–ZnO interface, consequently modifying the C–C bonds [31]. The phonon subsystem that creates additional number of defect states also contributes to the reduction of crystallinity [41]. Higher intensity ZnO characteristic peaks of the VACNT–ZnO sample were observed at 437.0 and 326.0 cm^{-1} (Fig. 5(c)) compared to the ZnO–VACNT sample in Fig. 5(b), indirectly implying that this sample contains a larger amount of ZnO. A peak of E_1 (LO) at 567.6 cm^{-1} associated with the local vibration of impurities in the ZnO sample was also detected, which implies that the ZnO nanorods synthesised on the VACNT array contain structural defects [7]. Note that there was a peak detected at approximately 480 cm^{-1} (indicated by the red arrow in Fig. 5(b) and (c)) in both nanocomposite samples. This peak is the result of the interface phonon mode [42], as further confirmed through the absence of this particular peak in the pristine ZnO sample.

3.4. Field electron emission performance

Fig. 6(a) show the *J–E* curves for all samples. The turn-on and threshold field of the VACNTs sample was found to be 2.66 and 3.18 V μm^{-1} at the current density of 1.00 and 10.00 μA cm^{-2}, respectively. Meanwhile, the turn-on field of pristine ZnO was 5.18 V μm^{-1}, twice that of the VACNTs. However, the threshold field of the ZnO could not be determined because the maximum current density of the sample was only 1.19 μA cm^{-2} at an applied field of 5.40 V μm^{-1}. In the case of the ZnO–VACNT nanocomposite sample, the turn-on and threshold field reduced to 1.60 and 2.03 V μm^{-1}, respectively. Meanwhile, for the VACNT–ZnO sample, the turn-on and threshold field is the lowest among the others, with values of 0.49 and 1.41 V μm^{-1}, respectively.

In terms of the current density, on one hand, the ZnO–VACNT nanocomposite resulted in 259.80 μA cm^{-2} and was slightly higher than the pristine VACNTs (212.85 μA cm^{-2}). On the other hand, the maximum current density from VACNT–ZnO nanocomposite is significantly higher than that of the other samples, with a value of 2090.00 μA cm^{-2}. The tremendous increase in the emission current demonstrates that the current enhancement is primarily contributed by the field emission of the VACNT–ZnO nanocomposite structure. The reductions in turn-on and threshold fields as well as the increase in the current emission for both nanocomposite samples demonstrate the improvement of the field FEE properties of the VACNTs. Therefore, it can be deduced that the addition of ZnO as a composite material to the pristine VACNTs can significantly improve the field emission properties of VACNTs.

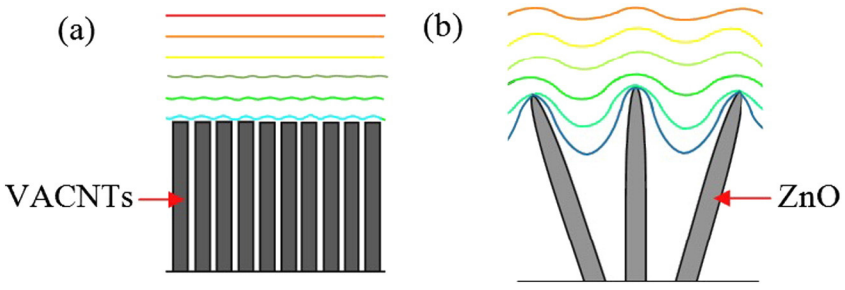

Fig. 8. Schematic plot of the equipotential lines of the electrostatic voltage for VACNTs and ZnO nanorods, demonstrating the screening effect as a result of dense VACNTs.

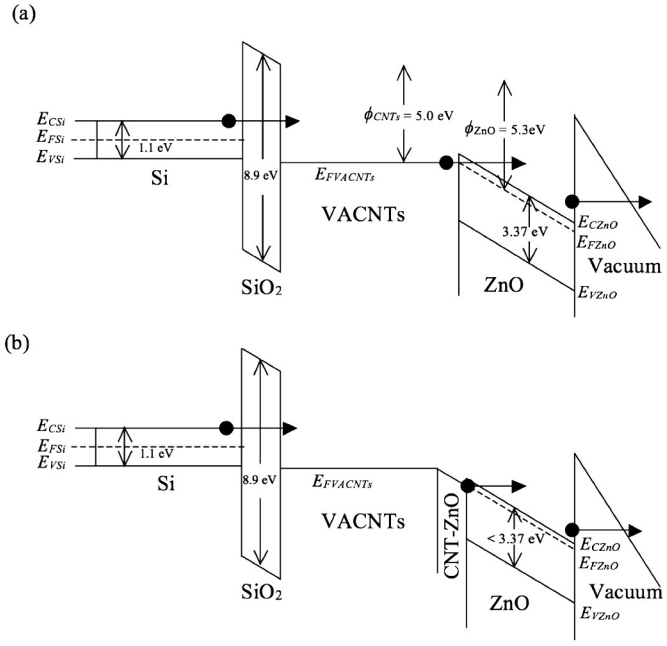

Fig. 9. Schematic band diagram of the VACNTs–ZnO nanocomposite (a) before and (b) after annealing, illustrating the reduction of the Schottky barrier height and the ZnO band gap, and the formation of the CNT–ZnO alloy at the VACNT–ZnO interface.

For the ZnO–VACNT nanocomposite sample, the enhancement of FEE was due to the presence of the conductive layer under the VACNTs, as illustrated by the band diagrams in Fig. 7. This layer generally assists the transfer of electrons from the substrate to the VACNTs. Basically, the barrier d, i.e., the SiO_2 layer between the VACNTs and the substrate (Fig. 7(a)) was concurrently reduced with the addition of the ZnO layer. Due to the high synthesis temperature of the VACNTs (800 °C), covalent bonds were introduced between the Fe:ZnO layer and the VACNT interface [43], thereby forming a conductive alloy layer of Fe:ZnO-C (Fig. 7(b)). The presence of this conductive alloy reduces the barrier thickness between the VACNTs and the substrate, thereby facilitating an easier electron transfer. In addition, the underlying conductive alloy layer also has good thermal conductivity, which induces a rapid release of the heat introduced by high current emission, hence preventing the VACNTs from burning [44] and enhancing the FEE properties.

Meanwhile, for the VACNT–ZnO nanocomposite sample, the significant improvement of the FEE properties is mainly due to the geometrical shape of the emitters. As shown in the FESEM image depicted in Fig. 3(d), the as-grown ZnO nanorods protruding from the surface of the VACNT–ZnO have smaller diameters at the tips, thereby resulting in a high aspect ratio and consequently leading to a local field strengthening at the tip region, where $E_{local} = \beta E$ [7]. Moreover, the ZnO array are in multifarious directions and have an optimal density for preventing the screen effect, which often occurs for the dense tips of a VACNTs emitter (Fig. 8) [2].

It is revealed that the improvement of the FEE is also correlated with the tunnelling effect of electrons through the VACNT–ZnO nanocomposite, as illustrated in Fig. 9. The VACNT–ZnO junction can be considered as a metal–semiconductor junction due to the narrower band gap of the CNTs (approximately a few hundred milli-electron volts at room temperature) [45] in comparison to ZnO. Because ZnO has a higher work function (ϕ) value than CNTs, with values of 5.3 and 5.0 eV, respectively, the junction formed is of an Ohmic nature. The electrons from the Fermi level of the VACNTs are injected to the conduction band of ZnO through tunnelling due to the existence of the Schottky barrier at the VACNT–ZnO junction (Fig. 9(a)).

However, the height of the Schottky barrier was reduced through the use of the high annealing temperature of 500 °C during the synthesis of ZnO on top of the VACNTs. The annealing process decreases the band gap of the ZnO [46], thus increasing the tunnelling probability. In addition, annealing at high temperature also introduces the formation of a conductive alloy at the VACNT–ZnO interface, which facilitates the electron transfer from the VACNTs to ZnO. The reduction of the ZnO band gap and formation of the VACNT–ZnO alloy at the interface is shown in Fig. 9(b). The VACNT array under the ZnO layer also play a significant role on the improvement of FEE by providing large connection areas between the ZnO to the Si substrate. This VACNT conductive layer does not limit the support to electron transfer, while helping to transfer the heat from the ZnO tips to the substrate, thereby protecting the emission tips from being destroyed by extensive heat generated through the high electric field [2].

The corresponding F–N plots of the samples were shown in Fig. 6(b). This plot was obtained according to the classical F–N equation:

$$\ln\left(J/E^2\right) = \ln\left(A\beta^2/\phi\right) - B\phi^{3/2}/\beta E$$

where J is the current density, E is the applied field, and ϕ is the work function (5 eV for carbon), A and B are constants ($A = 1.54 \times 10^{-6}$ A eV V^{-2} and $B = 6.83 \times 109$ $eV^{-3/2}$ V/m) and β is the field enhancement factor, which can be calculated using the slope of the linear part of the F–N plot. The calculated values of β, which were estimated from the F–N plot in the high field region, were found to be 6941, 1930, 6140, and 9977 for VACNTs, ZnO, ZnO–VACNT, and VACNT–ZnO, respectively. The significant increase in β for the VACNT–ZnO sample was attributed to the high aspect ratio and the optimal density of ZnO nanorods on the surface of the VACNT array, which reduced the screening effect [2]. The significant increase in β for the VACNT–ZnO sample was proportional to the geometrical parameters of the field emitter, being mainly related to its surface morphology and optimal density of the substrate [7].

The F–N plots of all the samples were found to demonstrate some deviations at the low electric field region, hence resulting in two linear segments. These deviations are attributed to several factors including surface adsorption in the low electric field region [47] or activation of abnormally active emission sites at the high electric field [48]. The deviation of the F–N plot that led to the existence of two linear segments also can be explained by using the double-barrier model [49], as illustrated by the band structure of the cathode in Fig. 10. Generally, there is a barrier between the VACNTs and the substrate [50]. The double-barrier model describes the process of electron transportation as occurring in two steps. First, an electron tunnels through the barrier between the Si substrate and VACNTs; second, the electron tunnels from the VACNTs to vacuum.

In equilibrium condition (without external bias), the Fermi levels are lined up (Fig. 10(i)). There are two barriers presented, namely (1) the Si substrate-VACNT interface barrier and (2) the VACNT–vacuum barrier. The finite separation between the Si substrate and VACNTs is due to the SiO_2 layer, which acts as an insulator. When an external voltage is applied, the Fermi levels are no longer lined up consistently. The Fermi levels shift with a magnitude that is a function of the applied voltage. The field penetration generated by the applied electric field induces the surface charge and causes the band bending of the SiO_2 conduction band [51].

At a low electric field, such that $0 < qV_{junction} < \phi_o$, where ϕ_o is assumed to be the barrier height of the junction, most electrons must tunnel through Barrier 1, i.e., the SiO_2 layer with width d. In this low electric field range, the contact resistance would be approximately constant as the voltage increases, and therefore, the tunnelling probability would hardly increase [52]. This behaviour could correspond to the occurrence of direct tunnelling [13], as the conduction band of the SiO_2 is higher than the Fermi level of the VACNTs (Fig. 10(ii)). Meanwhile, at Barrier 2, which is the VACNT–vacuum barrier, the electrons tunnel through the barrier by means of F–N tunnelling.

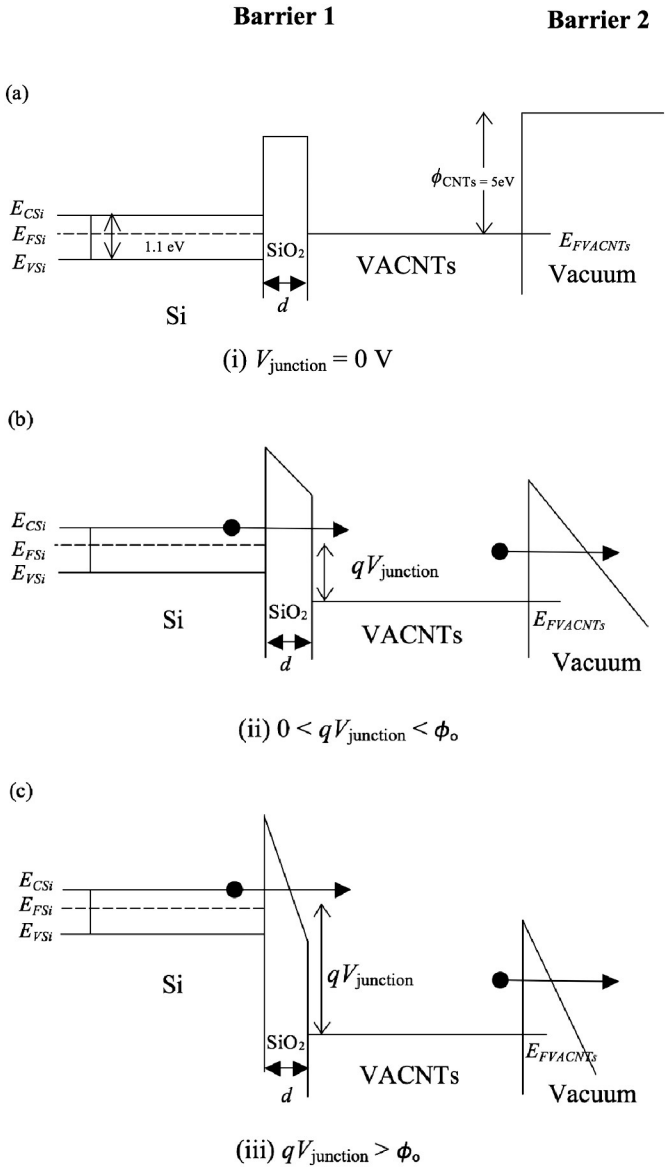

Fig. 10. Band structure of the cathode, illustrating the double-barrier model under different bias conditions. (a) In equilibrium condition i.e., without external bias; (b) at a low electric field, in which direct tunnelling occurred at Barrier 1, while F–N tunnelling occurred at Barrier 2; and (c) at a high electric field, in which F–N tunnelling occurred through both Barriers 1 and 2.

As the applied voltage increases further, i.e., $qV_{junction} > \phi_o$, the conduction band of the SiO_2 continuously bends, resulting in the conduction band being lower than the Fermi level of Si (Fig. 10(iii)). Hence, as the voltage increases, the effective barrier width *d* for the electron tunnelling becomes narrower. The contact resistance was therefore decreased rapidly, resulting in the increase in the tunnelling probability. At this point, F–N tunnelling occurs. This F–N tunnelling continues to occur at Barrier 2. Therefore, the tunnelling mechanism throughout the entire voltage range can be simplified with the following condition: at the low voltage range, the electron tunnels through the barrier between the Si substrate and VACNTs through direct tunnelling and tunnelling through the VACNTs to vacuum via F–N tunnelling; for high voltage, an electron tunnels through F–N tunnelling throughout all the barriers.

The deviating points in the F–N plot for all the samples (Fig. 6(b)) are denoted by * symbols. The * symbol indicates the critical field, which characterises the barrier thickness of the insulator layer between the structure and the substrates [13]. The F–N plot of the VACNTs, ZnO and VACNT–ZnO shows a deviation at closely spaced electric field values of 3.4, 3.8, and 3.5 Vμm^{-1}, respectively. These similar values are attributed to the same barrier, i.e., SiO_2, existing between the substrate and the structure. Meanwhile, the ZnO–VACNT sample shows a deviation at 2.0 Vμm^{-1}, which indicates a smaller barrier thickness of the insulator layer between the substrate and the VACNTs. This smaller barrier thickness is a result of the existence of the Fe:ZnO-C conductive layer between the substrate and VACNTs, as illustrated in Fig. 7. Furthermore, the small barrier thickness indicates a lower contact resistance and hence enables easier electron transfer. The enlarged *J–E* plot of Fig. 6 (c) demonstrated dramatic increase in current from 1 μA cm^{-2} at 1.6 V μm^{-1} to 260 μA cm^{-2} at 3.0 V μm^{-1} for the ZnO–VACNT sample. Under the same conditions, the emission current density of pristine VACNTs was only approximately 6 μA cm^{-2}, which indicates that the field emission of ZnO–VACNT nanostructure increased by a factor of 40. Therefore, it is proven that the Fe:ZnO-C conductive layer plays an important role in improving the field emission of VACNTs.

4. Conclusion

In summary, the FEE properties of the VACNTs from waste chicken fat were successfully enhanced by fabricating the VACNTs with ZnO nanostructures. This work revealed that the VACNT–ZnO nanocomposite configuration tremendously improved the FEE properties of the VACNTs by lowering the turn-on and threshold fields to approximately 0.49 and 1.41 V μm^{-1}, respectively and increased the emission current from 212.85 to 2090.00 μAcm^{-2}. Meanwhile, the ZnO–VACNT nanocomposite also successfully reduced the turn-on and threshold fields of VACNTs to 1.60 and 2.03 V μm^{-1}, respectively and the emission current increased from 212.85 to 259.80 μAcm^{-2}. It is concluded that the order of the composite configurations plays a significant role in enhancing the FEE properties of VACNTs.

Supplementary data

Supplementary material.

Acknowledgements

The authors are grateful to the Kurita Water and Environment Foundation Grant, the Fundamental Research Grant Scheme (Grant code: 2015-0154-102-02), the L'Oréal-UNESCO for Women in Science Fellowship Grant (Grant code: 2014-0008-102-11), the Prototype Development Research Grant Scheme (Grant code: 2013-0097-102-32), the National Nanotechnology Directorate Division Research Grant (Grant code: 2014-0015-102-03), the MARA Innovation & Research Grant Scheme, UPSI and NIT for the financial support and access to facilities for this work.

References

[1] H. Hu, D. Zhang, Y. Liu, W. Yu, T. Guo, Vacuum 115 (2015) 70–74.
[2] X. Yan, B.K. Tay, P. Miele, Carbon 46 (2008) 753–758.
[3] D. Cai, L. Liu, AIP Advan. 3 (2013) 122103.
[4] Y.W. Heo, L.C. Tien, Y. Kwon, D.P. Norton, S.J. Pearton, et al., Appl. Phys. Lett. 85 (2004) 2274–2276.
[5] S. Zhang, Y. Zhang, S. Huang, H. Liu, P. Wang, et al., Carbon 49 (2011) 3835–3841.
[6] L. Xin, Z. Wei-Man, L. Wei-Hua, W. Xiao-Li, Chin. Phys. B. 24 (2015) 057102.
[7] Y.M. Ho, W.T. Zheng, Y.A. Li, J.W. Liu, J.L. Qi, J. Phys. Chem. C 112 (2008) 17702–17708.
[8] H.B. Lian, J.H. Cai, K.Y. Lee, Vacuum 84 (2010) 534–536.
[9] C.S. Huang, C.Y. Yeh, Y.H. Chang, Y.M. Hsieh, C.Y. Ku, et al., Diam. Relat. Mater. 18 (2009) 452–456.
[10] K. Yu, Y.S. Zhang, F. Xu, Q. Li, Z.Q. Zhu, Appl. Phy. Lett. 88 (2006) 153123.
[11] N. Liu, G. Fang, W. Zheng, X. Zhao, H. Long, J. Phys. Chem. C 115 (2011) 14377–14385.
[12] C. Li, G. Fang, L. Yuan, N. Liu, L. Ai, et al., Nanotechnology 18 (2007) 155702.
[13] J. Zhang, X. Wang, W. Yang, W. Yu, T. Feng, et al., Carbon 44 (2006) 418–422.
[14] A.B. Suriani, A.R. Dalila, A. Mohamed, M.H. Mamat, M. Salina, et al., Mater. Lett. 101 (2013) 61–64.

[15] A.B. Suriani, A.R. Dalila, A. Mohamed, I.M. Isa, A. Kamari, et al., Mater. Res. Bull. 70 (2015) 524–529.
[16] A.R. Dalila, A.B. Suriani, M.S. Rosmi, M.S. Azmina, R. Rosazley, et al., Adv. Mater. Res. 832 (2014) 798–803.
[17] M. Salina, M. Rusop, A.B. Suriani, R. Ahmad, Trans. Electron Mater. 13 (2012) 64–68.
[18] A.B. Suriani, R.N. Safitri, A. Mohamed, S. Alfarisa, I.M. Isa, et al., Mater. Lett. 149 (2015) 66–69.
[19] M.F. Malek, M.H. Mamat, Z. Khusaimi, M.Z. Sahdan, M.Z. Musa, et al., J. Alloy Cmpd. 582 (2014) 12–21.
[20] M.F. Malek, M.H. Mamat, M.Z. Musa, Z. Khusaimi, M.Z. Sahdan, et al., J. Alloy Cmpd. 610 (2014) 575–588.
[21] M.S. Azmina, A.B. Suriani, A.N. Falina, M. Salina, M. Rusop, Adv. Mater. Res. 364 (2012) 359–362.
[22] M.S. Azmina, A.B. Suriani, M. Salina, A.A. Azira, A.R. Dalila, et al., Nano Hybrids 2 (2012) 43–63.
[23] SAM Zobir, SA Bakar, S Abdullah, Z Zainal, SH Sarijo, et al., J. Nanomaterials 2012; 2012:451473.
[24] M.S. Shamsudin, A.B. Suriani, S. Abdullah, S.Y.S. Yahya, M. Rusop, J. Spectroscopy (2013) 167357.
[25] P. Mbuyisa, S.P. Bhardwaj, F. Rigoni, E. Carlino, S. Pagliara, et al., Carbon 50 (2013) 5472–5480.
[26] D. Lupu, A.R. Biris, F. Watanabe, Z. Li, E. Dervishi, et al., Chem. Phys. Lett. 473 (2009) 299–304.
[27] L. Liu, M. Ge, H. Liu, C. Guo, Y. Wang, et al., Colloid Surface A 348 (2009) 124–129.
[28] S. Baruah, J. Dutta, J. Sol–Gel Sci. Technol. 50 (2009) 456–464.
[29] C. Li, Z. Jin, H. Chu, Y. Li, J. Nanosci. Nanotechnol. 8 (2008) 4441–4446.
[30] B. Manoj, A.G. Kunjomana, Int. J. Electrochem. Sci. 7 (2012) 3127–3134.
[31] C.C. Lin, B.T.T. Chu, G. Tobias, S. Sahakalkan, S.S. Roth, et al., Nanotech. 20 (2009) 1–7.
[32] A.K. Zak, W.H. Abd Majid, M.E. Abrishami, R. Yousefi, Solid State Sci 13 (2011) 251–256.
[33] F. Xu, Y. Lu, Y. Xie, Y. Liu, Mater. Design 30 (2009) 1704–1711.
[34] F. Gao, X.Y. Liu, L.Y. Zheng, M.X. Li, Y.M. Bai, et al., J. Cryst. Growth 371 (2013) 126–129.
[35] A. Baranowska-Korczyc, A. Reszka, K. Sobczak, B. Sikora, P. Dziawa, et al., J. Sol–Gel SciTechnol. 61 (2012) 494–500.
[36] S. Chattopadhyay, T.K. Nath, A.J. Behan, J.R. Neal, D. Score, et al., J. Magn. Magn. Mater. 323 (2011) 1033–1039.
[37] L. Xu, X. Li, J. Cryst. Growth 312 (2010) 851–855.
[38] D. Fu, G. Han, Y. Chang, J. Dong, Mater. Chem. Phys. 132 (2012) 673–681.
[39] W. Fuxue, C. Xiaolong, Y. Dawei, Z. Zhaomin, X. Shaoqing, et al., J. Semicon. 35 (2014) 093004.
[40] R. Kumar, R.K. Singh, J. Singh, R.S. Tiwari, O.N. Srivastava, J. Alloy Compd. 526 (2012) 129–134.
[41] J. Ebothe IV, S.B. Kityk, B. Claudet, K.J. Plucinski, et al., Opt. Commun. 268 (2006) 269–272.
[42] C.L. Du, Z.B. Gu, M.H. Lu, J. Wang, S.T. Zhang, et al., J. Appl. Phys. 99 (2006) 123515.
[43] C.Y. Wang, S. Adhikari, Phys. Lett. A 375 (2011) 2171–2175.
[44] J.Y. Pan, C.C. Zhu, Y.L. Gao, Appl. Surf. Sci. 254 (2008) 3787–3792.
[45] J.W.G. Wildoer, L.C. Venema, A.G. Rinzler, R.E. Smalley, C. Dekker, Nature 391 (1998) 59–62.
[46] N.S. Kumar, K.V. Bangera, G.K. Shivakumar, Appl. Nanosci. 4 (2014) 209–216.
[47] C. Dong, M.C. Gupta, Appl. Phys. Letters 83 (2003) 159–161.
[48] P. Verma, P. Chaturvedi, J.S.B.S. Rawat, M. Kumar, S. Pal, M. Bal, J. Mater. Sci. Mater. Electron. 18 (2007) 677–680.
[49] M.J. Fransen, T.L. van Rooy, P. Kruit, Appl. Surf. Sci. 146 (1999) 312–327.
[50] J. Tersoff, Appl. Phys. Lett. 74 (1999) 2122–2124.
[51] L. Zhang, X. Liu, Z. Lian, X. Wang, G. Shen, et al., J. Mater. Chem C. 2 (2014) 3965–3971.
[52] Q. Ngo, D. Petranovic, H. Yoong, S. Krishnan, C.Y. Yang, Nanotechnology 1 (2003) 252–255.